

Dynamical Analysis of Friction Induced Vibration in a Precision Motion Stage with a Friction Isolator

Jiamin Wang

Department of Mechanical Engineering
Virginia Tech
Blacksburg, Virginia 24061, USA

Xin Dong

Department of Mechanical Engineering
University of Michigan
Ann Arbor, MI 48109, USA

Oumar Barry*

Department of Mechanical Engineering
Virginia Tech
Blacksburg, Virginia 24061, USA

Chinedum Okwudire

Department of Mechanical Engineering
University of Michigan
Ann Arbor, MI 48109, USA

ABSTRACT

Motion stages are widely used for precision positioning in manufacturing and metrology applications. However, nonlinear pre-motion friction can significantly affect their control performance and accuracy. This paper analytically studies the dynamical effect of a friction isolator (FI) proposed in previous studies, in which the beneficial effects of FI on improving the robustness, speed, and precision of the system have been experimentally demonstrated. A fundamental understanding of the dynamical effects of FI is achieved by applying linear analysis on a motion stage with and without FI under the effect of LuGre friction dynamics. The systems are studied with the implementation of PID controllers, which, in terms of practicability in motion control, provide more general observations than when only PD is implemented. Parametric analysis is carried out on the effect of control gains, FI design parameters, and LuGre friction parameters to thoroughly observe the eigenvalue and stability characteristics. Numerical simulation is then established to validate the analytical results and demonstrate the interesting dynamical phenomena with the involvement of LuGre friction, PID control, and the friction isolator in the motion stage system. Based on the results, fundamental analytical conclusions about the FI are reached, which also pave the road for future nonlinear studies.

1 Introduction and Background

Motion stages are used for precision positioning in a wide range of manufacturing and metrology-related processes, such as machining, additive manufacturing, and semi-conductor fabrication [1]. Mechanical bearings (e.g., sliding and especially rolling bearings) are commonly used in these precision motion stages due to their large motion range, high off-axis stiffness, and cost-effectiveness [1]. However, they experience nonlinear pre-motion (i.e., static) friction which adversely affects their positioning precision and speed, causing large tracking errors, long settling times, and stick-slip phenomena [2, 3, 4, 5, 6, 7, 8]. Compensation methods are often used to mitigate the undesirable effects of pre-motion friction, including high-gain feedback [5], model-based feedforward, and feedback controllers [4, 7, 9, 10]. However, high-gain controllers could easily lead to large overshoot and limit cycles while model-based compensation methods often suffer from robustness and stability problems due to the rapid and nonlinear changes of pre-motion friction, thus limiting their practicality [5].

The friction isolator¹(FI), also known as the compliant joint method, has recently been proposed as an effective and robust method for mitigating pre-motion friction [9, 10]. The idea is to connect the mechanical bearing to the moving table of a motion stage using a joint that is very compliant in the motion direction, thus effectively isolating the motion stage from the strong nonlinearities associated with pre-motion friction. To illustrate this, Fig. 1(a) shows a conventional motion stage with a mechanical bearing that is rigidly connected to the moving table. It should be noted that the pre-motion friction is

*Corresponding Author: obarry@vt.edu

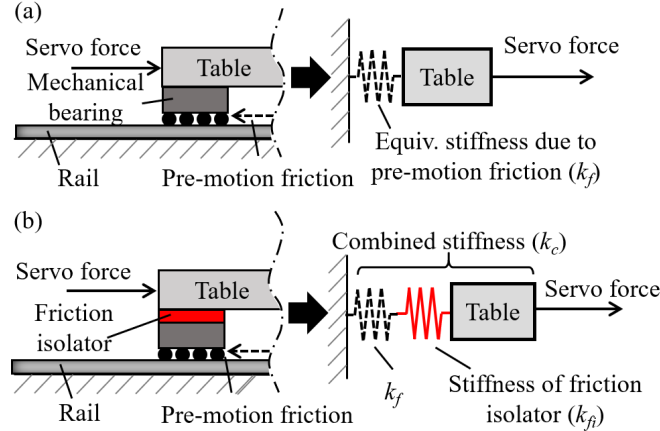


Fig. 1. Schematics of a precision motion stage with mechanical bearing attached to the table (a) rigidly and (b) using FI.

modeled as an equivalent spring of stiffness k_f connecting the table to the ground [2]. When the stage starts from rest (or after motion reversals), k_f rapidly reduces from its initially large value and eventually becomes zero, allowing full sliding/rolling of the stage. The highly nonlinear dynamics of pre-motion friction cause severely diminished positioning speed and precision of motion stages [2, 3, 4, 5, 6, 7, 8].

Figure 1(b) shows the concept of the FI for mitigating undesirable effects of pre-motion friction in precision motion stages [9, 10]. Rather than being rigidly attached to the moving table of the stage, the bearing is attached using a joint of stiffness k_{fi} , in the motion direction. Accordingly, the stage with the FI is modeled statically as a series combination of k_f and k_{fi} with combined stiffness $k_c = k_f k_{fi} / (k_f + k_{fi})$. Note that the bearing mass and damping of the FI are intentionally ignored here for the sake of simplicity; they are considered starting from Section 2. A very small k_{fi} dominates the combined stiffness felt by the servo controller when k_f is very large in the pre-motion regime; $k_c \rightarrow k_{fi}$ even when $k_f \rightarrow \infty$. Therefore, if $k_{fi} \ll k_f$ and k_{fi} is precisely known, accurate model-based compensation of pre-motion friction can be achieved even when a significant amount of error exists in k_f (due to low-fidelity friction modeling or variations of friction). Prior works [9] have experimentally demonstrated large reductions of tracking errors using low-fidelity friction models, with very high robustness in the presence of variations in k_f . Moreover, it has also been experimentally shown that the motion stage with the FI achieves a significantly reduced settling time compared to the conventional stage (i.e., without the FI) [10].

However, the introduction of the FI to a motion stage leads to nonlinear interactions between friction, the servo controller, and the FI dynamics. These interactions can be linked to friction-induced oscillation [6, 12, 13, 14, 15, 16, 17]. Given the remarkable experimental improvements in positioning precision, speed, and robustness brought by the FI, it is of interest to fundamentally understand the beneficial and potentially harmful effects of its dynamics on precision motion stages. This paper discusses the effects of the FI on the motion stage system using a PID controller and LuGre friction through linear analysis and numerical simulation, which is an extension of [18]. The major objectives of this study are to understand:

- (O1) The effects of friction parameters on the stability of motion stage control systems (both with and without FI).
- (O2) The similarities and differences in dynamical behaviors between the motion stages with and without FI.
- (O3) The accordance between the linear stability analysis and numerical results from the nonlinear dynamical simulation, and the nonlinear phenomena not indicated by the linear analysis.

The content of the paper is as follows: in Section 2, we review relevant works on friction-induced oscillation and highlight the similarities and differences in which they do not address the dynamics of a servo-controlled motion stage with an FI; section 3 discusses the dynamical model of the systems with and without FI based on the LuGre friction model; in Section 4, we parametrically study and compare the stability of the PID-controlled motion stages with and without FI based on linear stability analysis; in Section 5, we use numerical simulations to validate the linear stability results and demonstrate other interesting phenomena associated with the addition of the FI; and the conclusions and future research directions are discussed in Section 6.

2 Review of Related Literature

Figure 2(a) shows a rudimentary dynamical model of a servo-controlled motion stage with the FI. The moving table of mass m_t is connected to the tracking reference "wall" r by stiffness k_p and damping k_d , which also respectively represent

¹The term *friction isolator* is, on rare occasions, used as shorthand for *friction-pendulum isolator* in the literature, e.g., [11]. However, the friction-pendulum isolator is a vibration isolator that uses Coulomb friction for damping, not a device that isolates a system from deleterious effects of friction, as is the case with the friction isolator discussed here.

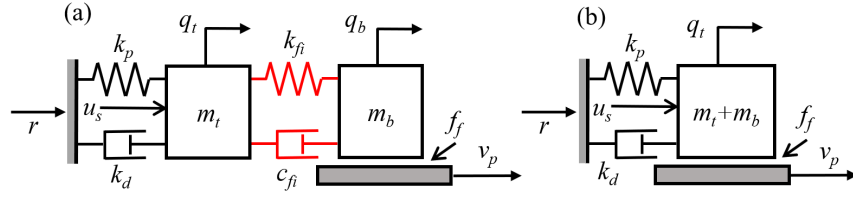


Fig. 2. Dynamical models of a servo-controlled stage (a) with and (b) without the FI.

the proportional (P) and derivative (D) gains of the servo controller regulating the tables position (i.e., q_t). A supplemental control force u_s is added to account for any additional servo forces that may be applied to the table (e.g., feedforward force, integral action). The FI is modeled as a mass m_b connected to m_t via stiffness k_{fi} and c_{fi} ; note that mass m_b accounts for the combined mass of the FI and mechanical bearing attached to it, whose position is defined by q_b . Friction force f_f is applied to m_b via a moving platform whose motion is prescribed by v_p .

Figure 2(b) shows a servo-controlled stage without FI. Notice that the PD-controlled stage (i.e., $u_s = 0$) without the FI represents a one degree-of-freedom (DOF) friction oscillator, which has been studied extensively in the literature in the context of friction-induced vibration with self and/or external excitations [12, 13]. Studies on friction oscillators have typically been performed using static friction models (e.g., dry friction). However, dynamical models that include the nonlinear stiffness characteristics of pre-motion friction have been adopted in some studies to capture the smooth transitions between stick and slip that are commonly observed in experiments [6, 14]. Effects of different servo controllers (e.g., integral action) on the dynamics and stability of the 1-DOF friction oscillator have been investigated in [6, 15].

The 1-DOF oscillator has also been extended to multiple DOFs for investigating the effects of mode coupling or obtaining generalized characteristics of the system [14, 16, 17]. However, these multi-DOF models either include an orthogonal DOF or simply connect several oscillators in series, with friction acting on each oscillator. This is unlike the FI shown in Fig. 2(a) where friction only acts on the bearing (m_b) not on the moving table (m_t). The closest work that adopts a similar configuration as that shown in Fig. 2(a) is [17], in which a 2-DOF model is used to study the stick-slip characteristics of the friction oscillator with tangential contact compliance. However, a Coulomb model that only captures dry friction is used for analysis in [17]; the highly nonlinear behavior of pre-motion friction is ignored. Moreover, the model in [17] does not include the effects integral controller that is widely implemented on precision motion stages. Therefore, the rest of this paper is intended as a first step in addressing the deficiencies of prior work on friction oscillators in the context of servo-controlled motion stages with the FI.

3 Dynamical Model of Motion Stage with Friction

This section introduces the dynamical models of servo controlled motion stages with and without FI, as shown in Fig.2. For simplicity of labeling, the motion stage without FI is referred to as System α and the motion stage with FI is referred to as System β hereinafter.

3.1 The LuGre friction model

A variety of friction models have been proposed in the past decades. In this study, the LuGre friction model [19, 14] is adopted, which incorporates viscous friction, pre-sliding, and hysteresis behaviors. The LuGre model introduces an internal state z governed by the dynamics

$$\dot{z} = v - a_z(v)z \quad (1)$$

with

$$a_z(v) = \frac{|v|}{g(v)}; \quad g(v) = \frac{f_k}{\sigma_0} = \frac{f_c + (f_s - f_c)e^{-(v/v_s)^2}}{\sigma_0} \quad (2)$$

where f_k is the kinetic friction with the Stribeck structure; f_c is the Coulomb friction; f_s is the static friction; v_s is the Stribeck velocity threshold; and σ_0 is the initial contact stiffness of the bristle (i.e., initial pre-motion frictional stiffness is modeled as bristles with average deformation z). It should be noted that the kinematic friction model adopted in the LuGre model is the Stribeck friction model (excluding the viscous friction), which incorporates the transition from f_s to f_c with the increase of velocity. The friction force based on the LuGre friction dynamics is calculated as

$$f_f = \sigma_0 z + \sigma_1 \dot{z} + \sigma_2 v \quad (3)$$

where σ_1 is the micro-damping of the bristle, and σ_2 accounts for the macroscopic viscous friction. In terms of the *stick-slip* phenomenon, the performance of LuGre model has proved similar to that of the hybrid force models [20].

Observe that the dynamics of z is only affected by v . The equilibrium points of z can be reached only when

$$(1): v = 0 \quad \text{or} \quad (2): z = v/a_z(v) \quad (4)$$

Equilibrium (1) is known as the sticking equilibrium, and equilibrium (2) second is referred to as the slipping equilibrium. The fixed points for any dynamic systems that involves LuGre friction have to satisfy either of these two conditions. It should be noted that the dynamical model is a switched system at $v = 0$ due the existence of $\text{sgn}(v)$ and $|v|$.

3.2 Motion control system and its relevance to self-excitation

The models shown in Fig. 2 can be used to study the dynamics of a servo-controlled motion stage during trajectory tracking application. Trajectory tracking of motion stages is often realized with forces/torques generated by control algorithms based on the time varying reference $r(t)$ and control output y , which is defined for both systems as

$$y_\alpha = y_\beta = q_t \quad (5)$$

This leads to the definition of control error

$$\varepsilon = q_t - r(t); \quad (6)$$

Different controllers can be applied to the systems, including the PID feedback controller variants which have been widely implemented in industry. The standard linear PID controller has the structure of

$$u_b = -\varepsilon_i - k_p \varepsilon - k_d \dot{\varepsilon} \quad (7)$$

where $\varepsilon_i = k_i \int \varepsilon dt$; and $k_p, k_i, k_d \geq 0$ are respectively the proportional, integral, and derivative gain matrices. PD controller can be acquired by having $k_i = 0$. Note that k_p and k_d are equivalent to respectively k and c in Fig.2. Adopting PID controller will also introduce to the system an integral state $y_i = k_i \int q_t dt$, which is the integral of the output.

Based on the above setups, the states of the systems are defined as

$$x_\alpha = [q_t \quad \dot{q}_t \quad z \quad y_i]^T; \quad x_\beta = [q_t \quad q_b \quad \dot{q}_t \quad \dot{q}_b \quad z \quad y_i]^T \quad (8)$$

and the equations of motion of the two systems are

$$\dot{x}_\alpha = \begin{bmatrix} \dot{q}_t \\ (-f_f + u)/m_\alpha \\ v - a_z(v) \\ k_i q_t \end{bmatrix}; \quad \dot{x}_\beta = \begin{bmatrix} \dot{q}_t \\ \dot{q}_b \\ (f_{fi} + u)/m_t \\ (-f_{fi} - f_f)/m_b \\ v - a_z(v) \\ k_i q_t \end{bmatrix} \quad (9)$$

where

$$f_{fi} = k_{fi}(q_b - q_t) + c_{fi}(\dot{q}_b - \dot{q}_t) \quad (10)$$

is the coupling force of the friction isolator; $m_\alpha = m_t + m_b$ is the total mass of the system; and u is the control input. Furthermore, since the dynamical model of the machine is introduced as a motion control system, by defining

$$x_\alpha^* = [\varepsilon \quad \dot{\varepsilon} \quad z \quad \varepsilon_i]^T; \quad x_\beta^* = [\varepsilon \quad \varepsilon_b \quad \dot{\varepsilon} \quad \dot{\varepsilon}_b \quad z \quad \varepsilon_i]^T \quad (11)$$

where $\varepsilon_b = q_b - r$, the alternative representation of the systems in terms of the errors are

$$x_\alpha^* = \begin{bmatrix} \dot{\varepsilon} \\ (-f_f + u)/m_\alpha - \ddot{r} \\ v - a_z(v) \\ k_i \varepsilon \end{bmatrix}; \quad x_\beta^* = \begin{bmatrix} \dot{\varepsilon} \\ \dot{\varepsilon}_b \\ (f_{fi} + u)/m_t - \ddot{r} \\ (-f_{fi} - f_f)/m_b - \ddot{r} \\ v - a_z(v) \\ k_i \varepsilon \end{bmatrix} \quad (12)$$

A few studies [13, 14, 21, 22] in friction-induced vibrations have analyzed the cases where friction is introduced from a moving platform (e.g., belt, conveyor), shown in Figure 2. These types of systems are referred to as self-excitation systems, which lead to slightly different definitions of the relative velocity v

$$v_\alpha = \dot{q}_t - v_p; \quad v_\beta = \dot{q}_b - v_p \quad (13)$$

where v_p is the platform velocity. Based on the above error state setup, the relative velocities can also be represented with errors and references as

$$v_\alpha = \dot{\varepsilon} - v_r; \quad v_\beta = \dot{\varepsilon}_b - v_r \quad (14)$$

Table 1. Parameters used for simulation based on measured values from the motion stage

m_t [kg]	1	m_b [kg]	0.5
f_S [N]	6.5	f_C [N]	5.1
k_{fi} [N/m]	40,000	c_{fi} [Ns/m]	2
v_s [m/s]	0.0167	σ_0 [N/m]	2.2×10^6
σ_1 [Ns/m]	237	σ_2 [Ns/m]	14.2

where

$$v_r = v_p - \dot{r} \quad (15)$$

This demonstrates the relevance between the self-excitation model and the motion control model adopted in this paper. The self-excitation models can be viewed as having $r = 0$ that results in $\varepsilon = q_t$. Equivalently, identical error dynamic behaviors can be acquired by having $\dot{r} = -v_p$, where \dot{r} plays the role of v_p . Note that the acceleration term \ddot{r}_h in Eq.(12) also needed to be compensated, which can be realized by having

$$u = u_f + u_b; \quad u_f = m_\alpha \ddot{r}_h \quad (16)$$

where u_f is the feed-forward controller that drives the system based on the acceleration of the planned trajectory \ddot{r}_h .

4 Linear Stability Analysis

The stability of the system is changed when the additional dynamics of the FI are introduced into the system. In this study, the stability of the system is parametrically studied using linear analysis techniques (Hurwitz properties, eigenvalues, etc.) with respect to the controller, design, and friction parameters. The default design and friction parameters used in the following analysis are listed in Tab. 1, which are obtained from experimental measurements as shown in the Appendix. In addition, the default control gains and reference velocity are selected as:

$$k_i = 1e6 \text{ N/ms}; k_p = 2e4 \text{ N/m}; k_d = 2e2 \text{ Ns/m}; v_r = 10 \text{ mm/s} \quad (17)$$

If PD control is specified, $k_i = 0$ will be the automatic setup. Any other parameter changes during analysis will be specified.

4.1 Equilibrium points and state Jacobian matrices

As part of the stability analysis, the calculation of the state equilibrium points may vary with the state space representations of the system. For Systems α and β , the equilibrium is studied with respect to the error system Eq.(12) and the controller Eq.(16). As mentioned in the previous section, equilibrium of the system with friction can be reached only when either of the two conditions in Eq.(4) is satisfied. For the motion control system, the sticking equilibrium points can only be obtained when $v_r = 0$. When the PD controller is applied ($k_i = 0$), these equilibrium points are calculated as

$$x_{\alpha,0}^* = [\varepsilon_0 \ 0 \ -k_p \varepsilon_0 / \sigma_0 \ 0]^T \quad (18a)$$

$$x_{\beta,0}^* = [\varepsilon_0 (k_t \varepsilon_0 - m_b \ddot{r}_h) / k_{fi} \ 0 \ 0 \ -k_p \varepsilon_0 / \sigma_0 \ 0]^T \quad (18b)$$

where $k_t = K_p + k_{fi}$; and $\varepsilon_0 \in \mathbb{R}$ is the steady state position error. When $k_i \neq 0$, the sticking equilibrium points become

$$x_{\alpha,0}^* = [0 \ 0 \ -\varepsilon_{i,0} / (\sigma_0) \ \varepsilon_{i,0}]^T \quad (19a)$$

$$x_{\beta,0}^* = [0 \ (\varepsilon_{i,0} - m_b \ddot{r}_h) / k_{fi} \ 0 \ 0 \ -\varepsilon_{i,0} / \sigma_0 \ \varepsilon_{i,0}]^T \quad (19b)$$

where $\varepsilon_{i,0} \in \mathbb{R}$ is the integral error that balances the unmodeled system dynamics. Apparently, Eq.(19) shows elimination of the steady state position error by the PID controller, provided that the PID controller is stabilizing the system.

The slipping equilibrium occurs in Eq.(4) when $v_r \neq 0$, which leads to the equilibrium points of the systems under PD control as

$$x_{\alpha,0}^* = \begin{bmatrix} -f_{f,0} / k_p \\ 0 \\ h(v_r) \\ 0 \end{bmatrix}; \quad x_{\beta,0}^* = \begin{bmatrix} -f_{f,0} / k_p \\ \varepsilon_{b,0,pd} \\ 0 \\ 0 \\ h(v_r) \\ 0 \end{bmatrix} \quad (20)$$

where

$$h(v) = v / a_z(v) = \text{sgn}(v)g(v); \quad f_{f,0} = \sigma_0 h(v_r) + \sigma_2 v_r \\ \varepsilon_{b,0,pd} = -(k_t f_{f,0} + k_p m_b \ddot{r}_h) / (k_p k_{fi})$$

Similarly, the slipping equilibrium points for PID controllers can be calculated as

$$x_{\alpha,0}^* = \begin{bmatrix} 0 \\ 0 \\ f_{f,0} \\ -h(v_r) \end{bmatrix}; x_{\beta,0}^* = \begin{bmatrix} 0 \\ -(f_{f,0} + m_b \dot{v}_h)/k_{fi} \\ 0 \\ 0 \\ h(v_r) \\ -f_{f,0} \end{bmatrix} \quad (21)$$

Linear stability analysis of the system can be acquired by examining the Hurwitz properties of the state Jacobian matrix calculated by linearizing the system at the equilibrium points [23, 24]. Since the system is nonlinear, only local stability can be indicated by this method. As mentioned previously, the sticking equilibrium cannot be analyzed with such method since the signum function is not continuous when $v = 0$. For System α and $k_i = 0$, the state Jacobian matrix is

$$A_{\alpha} = \begin{bmatrix} 0 & 1 & 0 \\ -k_p/m_a & a_{\alpha,[2,2]} & a_{\alpha,v,z} \\ 0 & a_{\alpha,z,v} & -a_z(v) \end{bmatrix} \quad (22)$$

with the elements

$$\begin{aligned} a_{\alpha,[2,2]} &= -(k_d + \sigma_1 + \sigma_2 - \sigma_1 z(\partial a_z(v)/\partial v))/m_a \\ a_{\alpha,v,z} &= -(\sigma_0 - \sigma_1 a_z(v))/m_a \\ a_{\alpha,z,v} &= 1 - z(\partial a_z(v)/\partial v) \end{aligned} \quad (23)$$

where

$$\frac{\partial a_z(v)}{\partial v} = \frac{\text{sgn}(v)[g(v)v_s^2 + 2v^2(g(v) - f_c/\sigma_0)]}{g^2(v)v_s^2} \quad (24)$$

Since $z = h(v)$ at the equilibrium, the elements can be further simplified as

$$\begin{aligned} a_{\alpha,[2,2]} &= -(k_d + \sigma_2 - \sigma_1 \rho_f(v)v^2/v_s^2) \\ a_{\alpha,z,v} &= -\rho_f(v)v^2/v_s^2 \end{aligned}$$

where

$$\rho_f(v) = 2 - \frac{2f_c}{f_c + (f_s - f_c)e^{-(v/v_s)^2}} \quad (25)$$

is the ratio bounded in $(0, 2(f_s - f_c)/f_s]$. Similarly, for System β and $k_i = 0$, the Jacobian can be calculated as

$$A_{\beta} = \begin{bmatrix} 0 & 0 & 1 & 0 & 0 \\ 0 & 0 & 0 & 1 & 0 \\ a_{\beta,[3,1]} & k_{fi}/m_t & a_{\beta,[3,3]} & c_{fi}/m_t & 0 \\ k_{fi}/m_b & -k_{fi}/m_b & c_{fi}/m_b & a_{\beta,[4,4]} & a_{\beta,v,z} \\ 0 & 0 & 0 & a_{\beta,z,v} & -a_z(v) \end{bmatrix} \quad (26)$$

where

$$\begin{aligned} a_{\beta,[3,1]} &= -(k_{fi} + k_p)/m_t \\ a_{\beta,[3,3]} &= -(c_{fi} + k_d)/m_t \\ a_{\beta,[4,4]} &= -(c_{fi} + \sigma_2 - \sigma_1 \rho_f(v)v^2/v_s^2)/m_b; \\ a_{\beta,v,z} &= -(\sigma_0 - \sigma_1 a_z(v))/m_b; \\ a_{\beta,z,v} &= -\rho_f(v)v^2/v_s^2 \end{aligned} \quad (27)$$

Notice that the sign of v does not affect value of the state Jacobian matrices, which indicates the symmetry of the system. These matrices are only dependent on the states \dot{e} (System α), \dot{e}_b (System β), and z . At the slipping equilibrium points, $v = v_r$ will determine the value of the matrices. For the PID cases, the state Jacobian matrices can be redefined as

$$A_{\alpha,i} = \begin{bmatrix} 0 & [k_i \ 0 \ 0] \\ [0 \ 1/m_a \ 0]^T & A_{\alpha} \end{bmatrix} \quad (28)$$

and

$$A_{\beta,i} = \begin{bmatrix} 0 & [k_i \ 0 \ 0 \ 0 \ 0] \\ [0 \ 0 \ -1/m_t \ 0 \ 0]^T & A_{\beta} \end{bmatrix} \quad (29)$$

which are acquired through rearranging the sequence of the states (moving ε_i to the first state).

Finally, it is sometimes helpful to convert the dimensional Jacobian matrix to non-dimensional form so that the eigenvalues are scaled for better observation. The general procedure is to select a principal natural frequency ω_n and corresponding non-dimensional time $t_n = \omega_n t$. In this study, the principal natural frequency for the two systems are selected as

$$\omega_{n,\alpha} = \sqrt{k_p/m_\alpha}; \quad \omega_{n,\beta} = \sqrt{k_p/m_t} \quad (30)$$

therefore, the non-dimensional state Jacobian matrices of the systems can be simply acquired by

$$A_{n,\alpha,i} = \Omega_{n,\alpha,1} A_{\alpha,i} \Omega_{n,\alpha,2} \quad (31a)$$

$$A_{n,\beta,i} = \Omega_{n,\beta,1} A_{\beta,i} \Omega_{n,\beta,2} \quad (31b)$$

where

$$\begin{aligned} \Omega_{n,\alpha,1} &= \text{diag}([1 \ \omega_{n,\alpha}^{-1} \ \omega_{n,\alpha}^{-2} \ \omega_{n,\alpha}^{-1}]) \\ \Omega_{n,\alpha,2} &= \text{diag}([\omega_{n,\alpha}^{-1} \ 1 \ \omega_{n,\alpha} \ 1]) \\ \Omega_{n,\beta,1} &= \text{diag}([1 \ \omega_{n,\beta}^{-1} \ \omega_{n,\beta}^{-1} \ \omega_{n,\beta}^{-2} \ \omega_{n,\beta}^{-2} \ \omega_{n,\beta}^{-1}]) \\ \Omega_{n,\beta,2} &= \text{diag}([\omega_{n,\beta}^{-1} \ 1 \ 1 \ \omega_{n,\beta} \ \omega_{n,\beta} \ 1]) \end{aligned} \quad (32)$$

The stability implied by the non-dimensional Jacobian matrices are identical to that from the dimensional ones.

4.2 Properties of state Jacobian matrices

Linear stability requires the state matrix to be Hurwitz, i.e., all eigenvalues have negative real parts. This can be evaluated numerically by directly calculating the eigenvalues or implementing Routh-Hurwitz criterion [23] on the characteristic equations calculated from the state Jacobian matrices. For example, the characteristic equation of A_α can be calculated as

$$s^3 + b_1 s^2 + b_2 s + b_3 = 0 \quad (33)$$

where the solution for s are the eigenvalues, and

$$\begin{aligned} b_1 &= a_z(v) + [k_d + \sigma_2 - \sigma_1 \rho_f(v) v^2 / v_s^2] / m_\alpha \\ b_2 &= [k_p + k_d a_z(v) + \sigma_2 a_z(v) - \sigma_0 \rho_f(v) v^2 / v_s^2] / m_\alpha \\ b_3 &= a_z(v) k_p / m_\alpha \end{aligned} \quad (34)$$

If the condition $b_1 b_2 > b_3$ can be reached, the linear stability at the equilibrium point can be acquired. While analytical evaluation of the Hurwitz property is very difficult due to the complexity of the system, for System α under PD control, it can be realized that when $\sigma_0 \rightarrow \infty$, other coefficients may have trivial effect on the stability of the system which leads to $b_1 \sim a_z(v)$, resulting in the stability condition as

$$b_1 b_2 - b_3 \sim \frac{a_z^2(v)}{m_\alpha^2} (k_d + \sigma_2 - \frac{|v|(f_S - f_C) e^{-(\frac{v}{v_s})^2}}{v_s^2}) > 0 \quad (35)$$

This indicates that when $\sigma_0 \rightarrow \infty$, the effect of micro-damping σ_1 will diminish. Smaller v_s in this case will require larger k_d or σ_2 to stabilize when v is close to v_s . For a fixed v_s , the minimal requirement for k_d and σ_2 to stabilize the system reaches its maximum when $v = v_s / \sqrt{2}$ (calculated from the derivative of $|v|(f_S - f_C) e^{-(v/v_s)^2} / v_s^2$ with respect to v), which indicates that the worst instability introduced by the friction may not occur at the Stribeck velocity.

Some other properties of the systems can also be acquired from the structure of the matrices. Notice that all the state matrices can be decomposed into

$$A = \begin{bmatrix} A_M & [0 \ \cdots \ 0 \ a_{v,z}] \\ [0 \ \cdots \ 0 \ a_{z,v}]^T & -a_z(v) \end{bmatrix} \quad (36)$$

where A_M is the submatrix corresponding to the states from the multibody system (which may include the integral state). For both systems, it can be observed that $\rho_f(v) \rightarrow 0$ when $|v| \gg v_s$. As a result, when the relative surface velocity is significantly larger than the Stribeck velocity threshold, $a_{z,v} \rightarrow 0$ and the eigenvalues of A consist of eigenvalues of A_M and $-a_z(v)$, the latter of which is negative automatically. This indicates that friction dynamics do not significantly affect the multibody dynamics when the surface velocity is large. The same conclusion can be achieved when $v_s \gg |v| > 0$ or $f_S \sim f_C$, which all lead to $a_{z,v} \rightarrow 0$. Based on this property, the analysis scope can be reasonable focused on the low speed range, which is critical in precision positioning.

Similarly, the structures of A_i indicate that, when k_i is small, the eigenvalues from A will be unaffected and remain in A_i . This property has made it convenient to distinguish the eigenvalue introduced from ε_i , which is zero when $k_i = 0$.

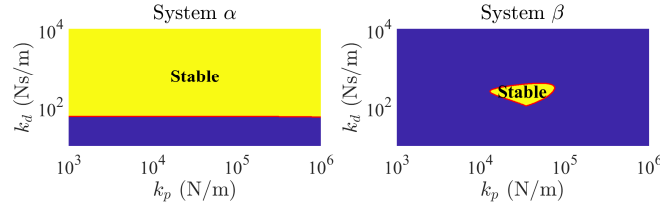


Fig. 3. Region of stable PD gain for System α and β at $v_r = 10$ mm/s, where the red contour is the boundary of the stable domain.

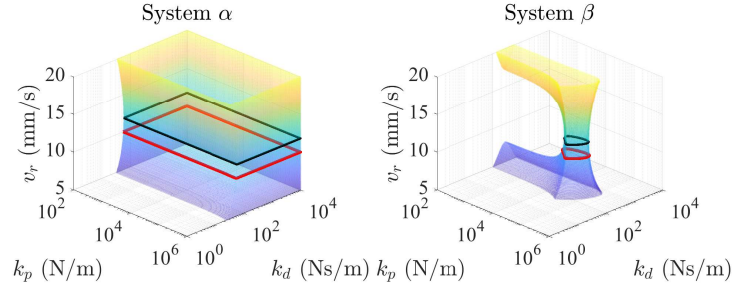


Fig. 4. The evolution of the boundary of the stable PD gain domain with respect to v_r for both systems, where the red contour is the boundary at $v_r = 10$ mm/s (also observable in Fig.3), and the black contour is the boundary at $v_r = v_s/\sqrt{2} \sim 11.8$ mm/s

4.3 Effects of friction parameters on control stability

The parametric analysis begins with studying the effects of friction parameters on the stability of the control gains. According to the LuGre friction, f_f is affected by a total of seven parameters - v , v_s , f_s , f_C , σ_0 , σ_1 , and σ_2 , among which only v is state dependent and related to motion control. Based on $v = v_r$ at the equilibrium points, the stability of the control gains in the domain of interest are inspected. In Fig.3, the ranges of stable PD control gain combination at the default reference velocity $v_r = 10$ mm/s is compared between System α and β . An apparent decrease in the stable gain region occurs when FI is applied. Similar observation is also shown in Fig.4, where the variation of the stable gain region boundary along v_r is presented. In general, the PD control gain selection are more narrow for System β . The general pattern of the boundaries has shown it is as predicted by Eq.(35) that in System α , k_d need to be larger than a certain value to overcome the instability effect by friction. The stability boundary at $v_r = v_s/\sqrt{2} \sim 11.8$ mm/s has also shown that the estimation of the worst case friction induced instability is valid when σ_0 is large. Figure 4 has also shown that the same patterns also apply for System β , which the smallest stable gain boundary also takes place at $v_r = v_s/\sqrt{2}$ with a large σ_0 . The boundary at the default v_r appear to be slightly larger in both cases.

The effect of friction parameters on the ranges of stable PID control gain is showcased in Fig.5. In most cases, an extremely large k_i will lead to instability, which is also applicable for the two systems in this study. For system α , it can be easily derived that $k_p(k_d + \sigma_2) > k_i$ is the stability criterion for PID control when the LuGre dynamics is decoupled (i.e., $|v_r| \gg v_s$ or $v_s \gg |v_r|$), which is as shown in the figure that simply increasing k_p and k_d allows employing larger k_i . The coupling of LuGre dynamics has significantly narrowed the originally similar stable gain regions of System β . The remaining

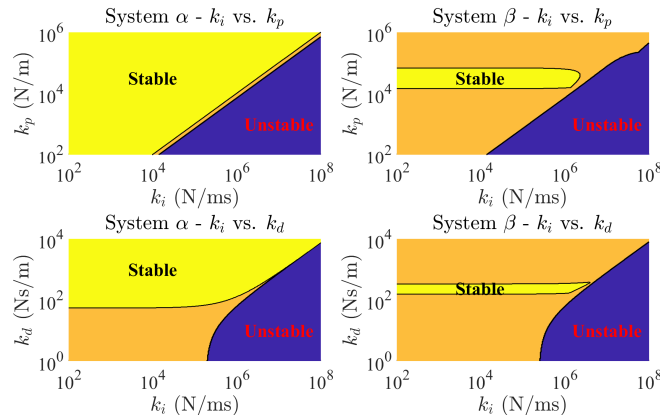


Fig. 5. Stability region of System α and β under PID control, where: yellow areas indicate stability for both $v_r = 10$ mm/s and $|v_r| \gg v_s$ (i.e. friction dynamics is isolated) cases; orange areas indicate instability for $v_r = 10$ mm/s but stability when $|v_r| \gg v_s$; and blue areas indicate instability for both $v_r = 10$ mm/s and $|v_r| \gg v_s$.

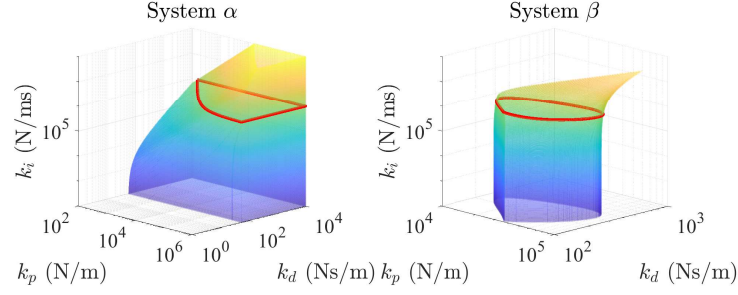


Fig. 6. The evolution of the boundary of the stable k_p - k_d domain with respect to k_i for both systems, where the red contour is the boundary at the default $k_i = 1e6$ N/ms.

stable area is predetermined by the stability of PD controller, which is hardly affected by a small k_i . It is also noticed that while the increase of k_i is reducing the stable PD gain domain, there is a shift in the center of stable region instead of direct decrease in the existing domain. This is demonstrated in Fig.6, where the development of the stable k_p - k_d boundaries with respect to k_i for both systems are presented. The results also indicate that the default k_i is hardly affecting the boundary.

Apart from v_r , the values of remaining friction parameters are usually difficult to precisely control in practice. The effects of some parameters are studied in groups by applying the constraints of $v_r = v_s$ and $f_S/f_C = 6.5/5.1$. As a result, scaling up v_r will be equivalent to scaling up v_s , or scaling down f_S or f_C . Since the effect of friction in System α has been largely predicted in Section 4.2, the boundaries of the stable k_p - k_d domain with the fixed default k_i are showcased in Fig.7 for System β only, where it can be clearly noticed that increasing v_s (or equivalently decreasing f_S and f_C) and σ_2 has led to better system stability. Provided the default friction parameters, while σ_1 appears to be playing a negative role in system stability. The most interesting phenomenon occur in the plot of σ_0 , as the boundary cease to change along after σ_0 has become extremely large. This indicates a pattern similar to one observed in System α has taken place, where an extremely large bristle stiffness σ_0 will diminish the effects of micro-damping σ_1 as described by Eq.(35). The effects of friction on stability in this case will be determined by the parameters excluding σ_0 and σ_1 .

As a short conclusion, the patterns of friction parameters are similar in systems both with and without FI, although the reduction of stable PID gain region in the System β due to the coupling of LuGre dynamics is significant. This indicates that the design of FI and the mass distribution are critical to the stability of the system, which leads to upcoming study on the effects of the design parameters.

4.4 Stability analysis on design parameters

An interesting phenomenon observed in the previous subsection is the unstable-stable-unstable transition along k_p or k_d respectively. To further inspect into this phenomenon, the eigenvalues of the systems are evaluated based on root locus. Based on the selected parameters, it is observed that in both systems there are:

- (1) An eigenvalue λ_i introduced by ϵ_i which satisfies $\lambda_i = 0$ at $k_i = 0$.
- (2) A negative real eigenvalue λ_z with relatively large magnitude introduced by z .

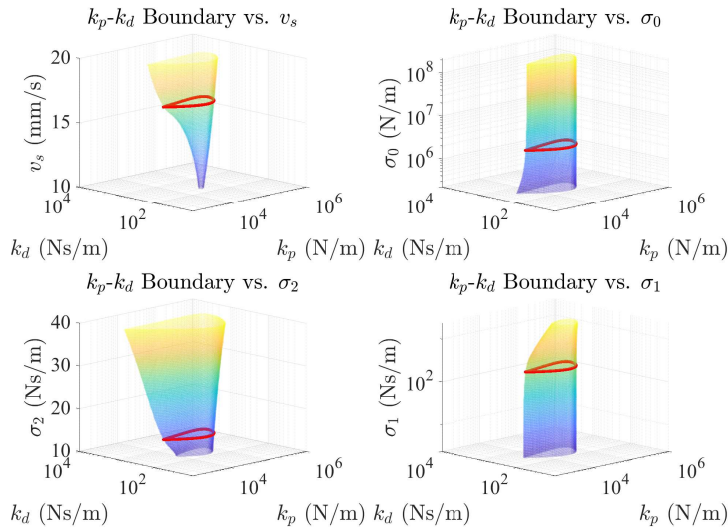


Fig. 7. The development of boundary of the stable k_p - k_d region with respect to different friction parameters for System β with $v_r = 10$ mm/s and $k_i = 1e6$ N/ms, where the red contour is the boundary at the default friction parameters.

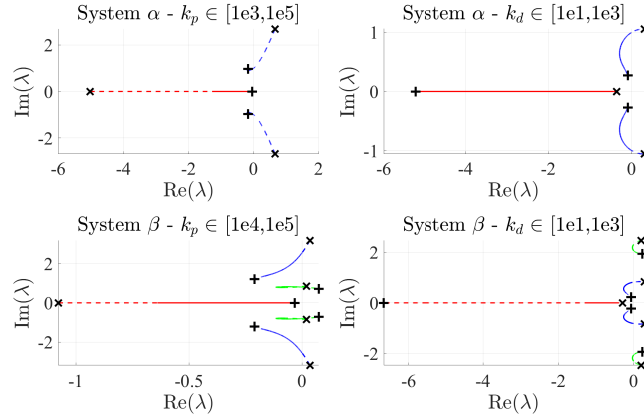


Fig. 8. Non-denaturalized root locus of System α and β with respect to k_p and k_d with $v_r = 10$ mm/s and $k_i = 1e6$ N/ms, where: different colors are used to distinguish eigenvalues; the dash and solid lines indicate the range of the locus that are unstable and stable, respectively; the "x" and "+" markers respectively indicate the beginning and the end of the locus.

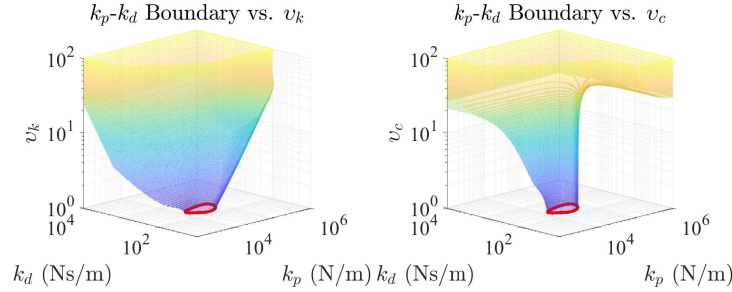


Fig. 9. The development of boundary of the stable k_p - k_d region with respect to v_k and v_c for System β with $v_r = 10$ mm/s and $k_i = 1e6$ N/ms, where the red contour is the boundary with the default parameters.

(3) Eigenvalues λ_t and λ_b (for System β only) in pairs introduced by the table and bearing (for System β only) respectively.

The root locus of System α is presented in Fig.8 with the default PID control gains. Since λ_c has a very large magnitude compared to the other eigenvalues, its trajectories has been excluded from the root locus. The figure has clearly demonstrated the transition from instability to stability with the increase of k_p and k_d . While it is hard to distinguish the remaining eigenvalues as they are coupled together, notice that the blue and red eigenvalue trajectories from System β are similar to those in the root locus of System α , and the additional eigenvalue trajectories in green has shown the unstable-stable-unstable transition as they both crossed the imaginary axis twice.

A possible case for stability to occur at extremely large k_p and k_d is that: the table has been equivalently "constrained" to the tracking reference, resulting in a loss of DOF that leads to remaining bearing as the only oscillating body similar to the case in System α , the stability of which as a result depends on k_{fi} and c_{fi} ; on the other hand, if k_{fi} and c_{fi} are extremely large, the table and bearing will be constrained together, which also returns System β to structure System α . Therefore, the effects from the FI design parameters are evaluated. By defining $v_k, v_c \in \mathbb{R}_+$, the new FI stiffness and damping can be scaled as $k_{fi} = v_k k_{fi,0}$ and $c_{fi} = v_c c_{fi,0}$, where $k_{fi,0}$ and $c_{fi,0}$ are the default values from Tab.1. The evolution of k_p - k_d boundary with respect to the the two scaling coefficients are presented in Fig.9. The result indicates that increasing k_{fi} and c_{fi} both help improving the range of stable PID control gains.

The stability of the system under the identical controller but with different design parameters is also studied, which is necessary as these parameters may change during usage. Similar to before, two new coefficients $v_t, v_b \in \mathbb{R}_+$ are defined

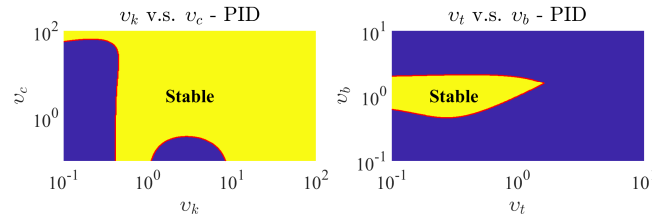


Fig. 10. Stability of the system at different design parameters with the default PID gains and v_r defined in Eq.(17), where the red contour is the boundary of the stable domain.

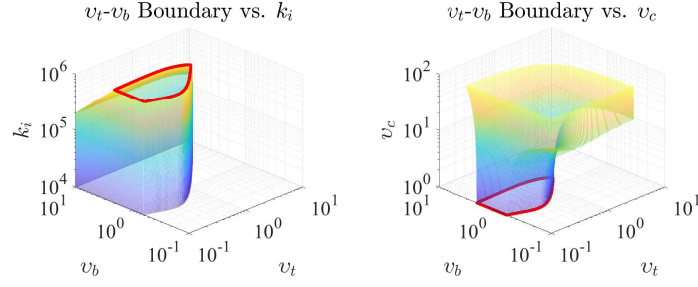


Fig. 11. The evolution of the boundary of stable v_t - v_b range with respect to k_i and v_c , where the red contour is the boundary with the default parameters observable from Fig.10.

so that the mass of the table and bearing can be scaled as $m_t = v_t m_{t,0}$ and $m_b = v_b m_{b,0}$ respectively. The result is shown in Fig.10, where the pattern in the v_k and v_c plots are agreeing with the previous conclusion of improving stability by increasing k_{fi} and c_{fi} . The results on v_t and v_b has shown that PID control can significantly narrow range of stable m_t - m_b combinations. This characteristic can apply limitation to the payload that the motion stage can handle. Through observations, it has been noticed that reducing k_i or increasing c_{fi} can significantly affect the result. This is shown in Fig.11, where it clearly shows that properly tuned k_i and c_{fi} allows more flexible mass distribution and payload handling.

In summary, the design parameters are essential to the stability of the system. Although the stability of the system can be improved by tuning certain parameters (especially increasing f_c), some of the values examined in the above analysis may not be reached in practice. The performed linear analysis can serve as useful reference in design optimizations.

5 Numerical Observations

A variety of numerical studies are established to be compared with the analytical results. Simulations are carried out with the built in ODE solver `ode45` in MATLAB, through which the nonlinearity of the systems can be observed. The initial conditions of the simulations are selected as $x_\alpha^* = [0, -v_r, 0, 0]^T$ and $x_\beta^* = [0, 0, -v_r, -v_r, 0, 0]^T$. The velocity-constant tracking reference is $r = v_r t$. The default parameters used in the simulation study are the system parameters from Tab. 1, the control gains in Eq.(17), and the reference velocity $v_r = 10$ mm/s.

The linear stability analysis results is first validated. The comparison between the analytical stability region of the PID control gains and its corresponding steady state oscillation error magnitude map acquire with numerical simulation is demonstrated in Fig.12. Notice that even in the numerical result, the stable area has been significantly separated from the unstable region with the visibly large difference in oscillation error. This indicates that the analytical and numerical results corroborate each other. While the numerical results do not imply the stability of the system as directly as the eigenvalues, more details in the behaviors of the system can be acquired from trajectories of the states.

The first observation focus on the time trajectory of $\dot{\epsilon}$ and $\dot{\epsilon}_b$. Non-dimensional time $t_n = \omega_n t$ has been used to provide a good time span for observation. The comparison of the controller under different k_i and k_d are presented in Fig.13. For both System α and β , trajectories (2) and (3) are both unstable; and for System β , trajectory (4) is unstable (refer to trajectory numbering in Fig.13 caption). These results corroborate the stability region in Fig.5. From the plots of System α , two types of instability have been observed, where the instability in trajectory (2) is caused by an extremely large k_i that will eventually lead $\dot{\epsilon}$ to infinity; and the one in trajectory (3) is the stick-slip phenomenon caused by the initial instability of the PD controller due to the coupling with friction that can be observed in Fig.3.

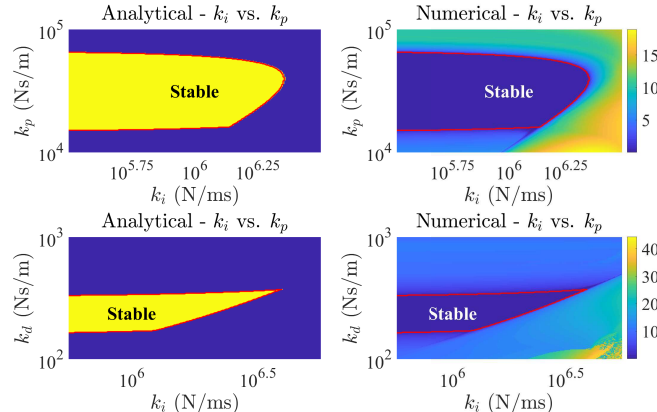


Fig. 12. The analytical stability region of PID control gains and its corresponding steady state oscillation error magnitude map acquired with numerical simulation.

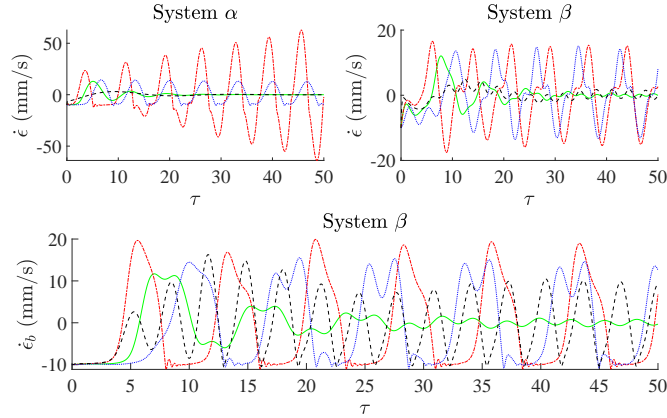


Fig. 13. Comparison of velocity error time trajectories ($v_r = 10$ mm/s) with different k_i and k_d for System α and β , where (1) green solid - default gains in Eq.(17), (2) red dot - changes in $k_i = 4.5e6$, (3) blue dash-dot - changes in $k_i = 1e5$ and $k_d = 2e1$, (4) black dash - changed to $k_d = 1e3$.

While the system are less stable when the FI with the default parameters is implemented, all of the instabilities in Fig.13 manifest as the stick-slip behaviors. The comparison of trajectory (2) in System α and β indicate that for certain control parameters, the implementation of the FI can prevent error from going unbounded, which can be a potential use of the device. While a large k_d has caused initial instability of the system as shown in trajectory (4), it can be observed that the corresponding $\dot{\epsilon}$ trajectory has a smaller oscillation error.

The time trajectories of the velocity errors with different design parameter scaling factors has also been observed in Fig.14. In general, the stability of different parameters has been well predicted by the linear stability analysis. It has been shown that with different v_k and v_c the system may perform a variety of behaviors. It is interesting to notice that the unstable oscillation in trajectory (4) does not show any pattern of stick-slip, while the instability is still related to LuGre friction dynamics. The results when varying v_t and v_b have shown the sensitive characteristics of the system towards the masses, since only trajectory (4) is stable even when the scaling factors are relatively small.

The above results imply that many instability behaviors of the system are bounded. Previous works [20,22] have studied limit cycles in the system with LuGre friction dynamics, which has also been observed in both System α and β . Based on different parameters, the limit cycles may possess different shapes. The phase portraits of the systems under different control gains are shown in Fig.15. For the first two sub-figures, the same parameters are used for Systems α and β . It should be noted that the limit cycle amplitude of System β is significantly smaller when implementing the FI. The corresponding time trajectories of the two limit cycles are also exclusively compared in Fig.16. This indicates the potential that FI, with certain parameters, can reduce the effect of friction-induced vibration that is transmitted into the table. Sub-figure (3) shows that chaotic behavior may be observed with certain parameters. Finally, sub-figure (4) demonstrates the limit cycle of the bearing states ϵ_b , where the stick-slip effect can be easily noticed.

The above numerical study has presented many interesting observations about the characteristics of the systems. While these results are in agreement with the stability analysis, many nonlinear features of the system, such as the cause of chaotic behaviors and the mechanics of reducing limit cycle amplitudes with the FI, will be further studied in future nonlinear research.

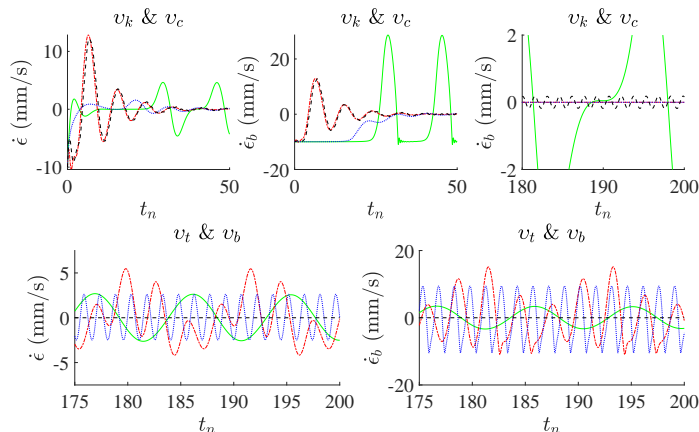


Fig. 14. Comparison of velocity error time trajectories ($v_r = 10$ mm/s) with different scaling factors v , where for v_k & v_c : (1) green solid - $v_k = 1e-1$, (2) red dot - $v_k = 1e1$, (3) blue dash-dot - $v_k = 1e-1$ and $v_c = 1e2$, (4) black dash - $v_k = 3$ and $v_c = 0.25$; and for v_t & v_b : (1) green solid - $v_b = 2$, (2) red dot - $v_t = 2$, (3) blue dash-dot - $v_b = 0.5$, (4) black dash - $v_t = 0.5$.

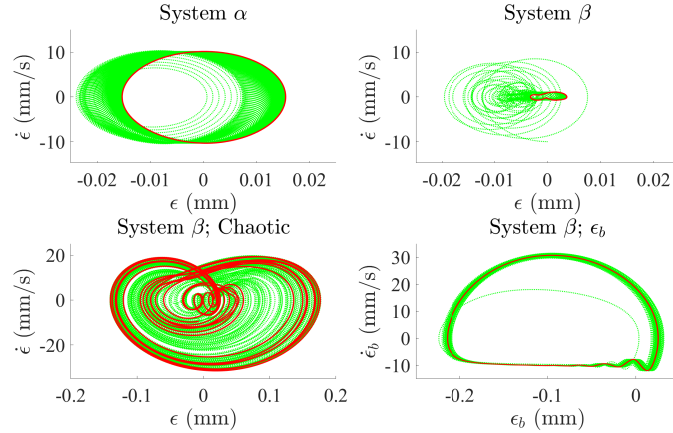


Fig. 15. Phase portraits and limit cycles (or chaotic behavior) highlighted in Solid Red Lines, where the control gains are (1) System α - $k_i = 1e6$, $k_p = 6.5e5$, $k_d = 2e1$; (2) System β - $k_i = 1e6$, $k_p = 6.5e5$, $k_d = 2e1$; (3) System β , Chaotic - $k_i = 8e6$, $k_p = 2e4$, $k_d = 2e2$; and (4) System β , ϵ_b - $k_i = 1e7$, $k_p = 2e4$, $k_d = 2e2$.

6 Conclusion and Future Work

This paper has examined the dynamics of a PID controlled motion stage system with an FI coupled with LuGre friction dynamics. Linear stability analysis has been performed on the slipping equilibrium point of the systems. The eigenvalues and stability of the system has been parametrically studied with respect to the PID control gains, FI design parameters, and friction parameters. Then a numerical analysis has been carried out to corroborate the analytical results and provide further insight into the behavior of the system. Thorough observations on the characteristics of the system have been acquired. Corresponding to the major objectives, the conclusions can be summarized as:

- (C1) Even with the implementation of FI, the effects of the friction parameters shares a lot of similar patterns as those observed in the rigid stage. For a fixed set of friction and FI parameters, the stability of the PID control is initially determined by the corresponding PD gains.
- (C2) The FI may introduce more instability to the system based on the parameter selections. The root locus has shown the unstable-stable-unstable transition in a pair of eigenvalues along with the increase of k_p and k_d . Large k_{fi} or c_{fi} may lead to larger ranges for stable PID gain selection. The stable domain of mass distribution is sensitive towards a few parameters. Lowering k_i and raising c_{fi} allows more flexible table-bearing ratio and larger payload capacity.
- (C3) Numerical validation shows that linear stability analysis around the slipping equilibrium is quite reliable in predicting the stability of the system. The numerical simulations show that installing the FI on a motion stage can potentially prevent the error from going unbounded and reduce the magnitude of limit cycles in unstable cases.

Based on these conclusions, the current work has laid a solid foundation for the upcoming research. The major directions of future work include:

- (1) Nonlinear dynamical analysis - the results of this paper are mainly limited to the scope of linear analysis. With nonlinear dynamical analysis, the behavior of the system can be studied with the involvement of higher order stiffness and damping. The stability of the system can also be studied more generally by including the switched dynamics around the sticking equilibrium points ($v = 0$).
- (2) Multibody and 3D system analysis - the current 2D dynamical models only contains at most two bodies. The investigation of system dynamics that contain multiple tables, the FI, and bearings from a 3D perspective can provide further insight into practical problems such as mode coupling and chaos.
- (3) Control algorithm development - the current study has revealed limitations in the traditional PID controllers. It is crucial to develop better controllers based on the understanding of the dynamics of the system, which will take into consideration the robustness, performance, and practical applicability.

Finally, the results from all these works will be tested and validated by comprehensive experiments.

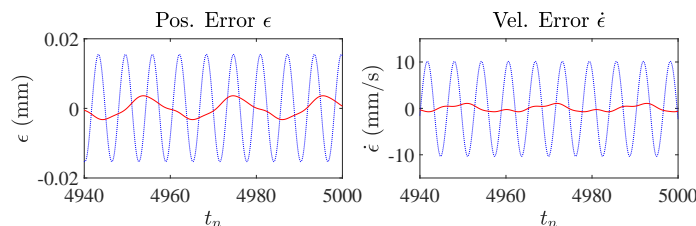


Fig. 16. Comparison of limit cycle time trajectories, where - (1) blue dot: System α , and (2) red solid: System β .

Acknowledgements

This work is funded by National Science Foundation (NSF) Award CMMI #1855390: Towards a Fundamental Understanding of a Simple, Effective and Robust Approach for Mitigating Friction in Nanopositioning Stages.

References

- [1] Altintas, Y., Verl, A., Brecher, C., Uriarte, L., and Pritschow, G., 2011. "Machine tool feed drives". *CIRP annals*, **60**(2), pp. 779–796.
- [2] Al-Bender, F., and Swevers, J., 2008. "Characterization of friction force dynamics". *IEEE Control Systems Magazine*, **28**(6), pp. 64–81.
- [3] Marques, F., Flores, P., Claro, J. P., and Lankarani, H. M., 2016. "A survey and comparison of several friction force models for dynamic analysis of multibody mechanical systems". *Nonlinear Dynamics*, **86**(3), pp. 1407–1443.
- [4] Futami, S., Furutani, A., and Yoshida, S., 1990. "Nanometer positioning and its micro-dynamics". *Nanotechnology*, **1**(1), p. 31.
- [5] Armstrong-Hélouvry, B., Dupont, P., and De Wit, C. C., 1994. "A survey of models, analysis tools and compensation methods for the control of machines with friction". *Automatica*, **30**(7), pp. 1083–1138.
- [6] Hensen, R. H., Van de Molengraft, M., and Steinbuch, M., 2003. "Friction induced hunting limit cycles: A comparison between the lugre and switch friction model". *Automatica*, **39**(12), pp. 2131–2137.
- [7] Maeda, Y., and Iwasaki, M., 2012. "Rolling friction model-based analyses and compensation for slow settling response in precise positioning". *IEEE Transactions on Industrial Electronics*, **60**(12), pp. 5841–5853.
- [8] Dong, X., Yoon, D., and Okwudire, C. E., 2017. "A novel approach for mitigating the effects of pre-rolling/pre-sliding friction on the settling time of rolling bearing nanopositioning stages using high frequency vibration". *Precision Engineering*, **47**, pp. 375–388.
- [9] Dong, X., Liu, X., Yoon, D., and Okwudire, C. E., 2017. "Simple and robust feedforward compensation of quadrant glitches using a compliant joint". *CIRP Annals*, **66**(1), pp. 353–356.
- [10] Dong, X., and Okwudire, C. E., 2018. "An experimental investigation of the effects of the compliant joint method on feedback compensation of pre-sliding/pre-rolling friction". *Precision Engineering*, **54**, pp. 81–90.
- [11] Mokha, A., Constantinou, M., Reinhorn, A., and Zayas, V. A., 1991. "Experimental study of friction-pendulum isolation system". *Journal of Structural Engineering*, **117**(4), pp. 1201–1217.
- [12] Oestreich, M., Hinrichs, N., and Popp, K., 1996. "Bifurcation and stability analysis for a non-smooth friction oscillator". *Archive of Applied Mechanics*, **66**(5), pp. 301–314.
- [13] Hinrichs, N., Oestreich, M., and Popp, K., 1998. "On the modelling of friction oscillators". *Journal of sound and Vibration*, **216**(3), pp. 435–459.
- [14] Hoffmann, N., 2007. "Linear stability of steady sliding in point contacts with velocity dependent and lugre type friction". *Journal of Sound and Vibration*, **301**(3-5), pp. 1023–1034.
- [15] Bisoffi, A., Da Lio, M., Teel, A. R., and Zaccarian, L., 2017. "Global asymptotic stability of a pid control system with coulomb friction". *IEEE Transactions on Automatic Control*, **63**(8), pp. 2654–2661.
- [16] Van de Vrande, B., Van Campen, D., and De Kraker, A., 1999. "An approximate analysis of dry-friction-induced stick-slip vibrations by a smoothing procedure". *Nonlinear Dynamics*, **19**(2), pp. 159–171.
- [17] Nakano, K., and Maegawa, S., 2009. "Stick-slip in sliding systems with tangential contact compliance". *Tribology International*, **42**(11-12), pp. 1771–1780.
- [18] Dong, X., Okwudire, C., Wang, J., and Oumar, B., 2019. "On the friction isolator for precision motion control and its dynamics". In Proceedings of the ASME 2019 International Design Engineering Technical Conferences (IDETC/CIE2019), American Society of Mechanical Engineers.
- [19] De Wit, C. C., Olsson, H., Astrom, K. J., and Lischinsky, P., 1995. "A new model for control of systems with friction". *IEEE Transactions on automatic control*, **40**(3), pp. 419–425.
- [20] Johanaström, K., and Canudas-De-Wit, C., 2008. "Revisiting the lugre friction model". *IEEE Control Systems Magazine*, **28**(6), pp. 101–114.
- [21] Li, Z., Ouyang, H., and Guan, Z., 2016. "Nonlinear friction-induced vibration of a slider–belt system". *Journal of Vibration and Acoustics*, **138**(4), p. 041006.
- [22] Saha, A., Wahi, P., Wiercigroch, M., and Stefański, A., 2016. "A modified lugre friction model for an accurate prediction of friction force in the pure sliding regime". *International Journal of Non-Linear Mechanics*, **80**, pp. 122–131.
- [23] Ogata, K., and Yang, Y., 2002. *Modern control engineering*, Vol. 4. Prentice-Hall.
- [24] Khalil, H. K. "Nonlinear systems". *Upper Saddle River*.
- [25] Hensen, R. H., van de Molengraft, M. J., and Steinbuch, M., 2002. "Frequency domain identification of dynamic friction model parameters". *IEEE Transactions on Control Systems Technology*, **10**(2), pp. 191–196.

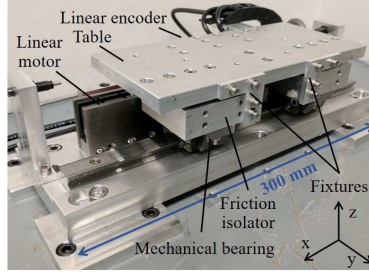


Fig. 17. Single-axis precision motion stage equipped with a FI; the fixtures can be used to deactivate FI.

Appendix: Identification of Friction Parameters

The parameters of LuGre model shown in Table 1 is identified on the in-house built precision motion stage of Figure 17. The stage has 1.5 kg moving mass and 40 mm travel range. It is guided by a pair of high-rigidity pre-loaded linear ball bearings. An air core linear motor is employed to drive the stage and the table position is measured using a linear encoder with a resolution of 4.88 nm. The FI prototype is used to attach each bearing to the moving table of the stage. The designed FI achieves orders of magnitude less stiffness than the initial large stiffness of pre-motion friction, i.e., $k_j \gg k_f$. In the meantime, it also maintains the same order of magnitude of off-axis stiffness (i.e., in y and z directions) as the mechanical bearing, so as not to unduly compromise the rigidity of the stage. Details about the design of the FI can be found in [9].

When friction is in the gross motion regime, the rate of bristle deflection is zero (i.e., $\dot{z} = 0$). This is when $z = h(v)$ at the slipping equilibrium, which results in the steady state friction force [19] as

$$f_{f,ss} = \sigma_0 h(v) + \sigma_2 v \quad (37)$$

The steady-state friction force $f_{f,ss}$ is obtained by commanding the stage to travel at different levels of constant velocity and measuring the linear motor force required to maintain the constant velocity motion. Figure 18 shows the measured $f_{f,ss}$ versus v curve which clearly exhibits the Stribeck effect. The related parameters (i.e., f_c , f_s , v_s , and σ_2) are identified using nonlinear least squares to fit the measured data.

The remaining parameters are identified using the simple model of an open-loop controlled stage with LuGre friction

$$\ddot{q}_t = (-f_f + u)/m_\alpha \quad (38)$$

where u is the input force. Linearizing the above equation and assuming friction is in the pre-motion regime (i.e., $q_t = z = 0$) yields [25]

$$\ddot{q}_t = -(\sigma_0 + (\sigma_1 + \sigma_2)\dot{q}_t - u)/m_\alpha \quad (39)$$

Using Laplace transformation, the frequency response function (FRF) from servo force to table displacement is obtained as

$$G(s) = \frac{1}{m_\alpha s^2 + (\sigma_1 + \sigma_2)s + \sigma_0} \quad (40)$$

The measured FRF (i.e., $G(s)$) is obtained by applying a constant-amplitude sinusoidal force input commands with varying frequencies to the servo motor and recoding the corresponding output displacement magnitudes of the tables position using the linear encoder. The parameters (i.e., σ_0 and σ_1) are obtained through least-square-fitting of the measured FRF with $m_\alpha = m_t + m_b = 1.5$ kg. As seen from Fig.19, the identified FRF matches closely with the measured one.

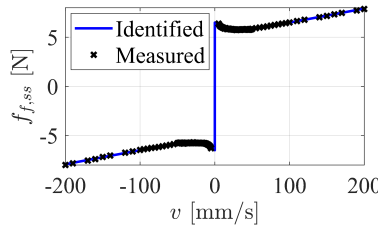


Fig. 18. Measured and identified $f_{f,ss}$ versus v curve

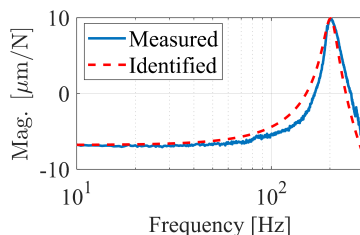


Fig. 19. Measured and identified magnitude plots using FRF from servo force to table displacement.